RSC Advances

PAPER

View Article Online
View Journal | View Issue

Cite this: *RSC Adv.*, 2017, **7**, 33869

New 10H perovskites $Ba_5Ln_{1-x}Mn_{4+y}O_{15-\delta}$ with spin glass behaviour†

Congling Yin, *[a] Genfang Tian,[b] Guobao Li,[c] Fuhui Liao[c] and Jianhua Lin[c]

Received 21st February 2017
Accepted 30th June 2017

DOI: 10.1039/c7ra02183f

rsc.li/rsc-advances

New 10H perovskite phases of composition $Ba_5Ln_{1-x}Mn_{4+y}O_{15-\delta}$ (Ln = Sm–Lu) have been synthesised by solid-state reactions at 1300 °C. Their crystal structures have been investigated using X-ray and neutron diffraction. The 10H perovskite structure has an ordered arrangement of Ln and Mn ions on the corner-sharing octahedral centres and the face-sharing octahedral centres respectively. MnO_6 octahedral distortions and short Mn–Mn distances have been identified in these structures, and oxygen vacancies are found in the c-BaO_3 layers. Additionally, magnetic measurements and neutron diffraction identify spin glass transitions in these new materials. These transitions are related to the Mn ions on the corner sharing octahedral sites, which mediate magnetic interactions between tetramers of MnO_6 octahedra.

Introduction

Interest in the physics of manganites has motivated investigation of the hexagonal perovskite $BaMnO_{3-\delta}$ system, which shows a variety of crystal structures and magnetic properties.[1–5] A series of polytypes (2H → 15R → 8H → 6H → 10H → 4H) have been identified in the $BaMnO_{3-\delta}$ system as the oxygen vacancy δ increases.[4,5] Further perovskite polytypes may be generated when Mn is replaced by other cations.

Many doped $BaM_xMn_{1-x}O_3$ systems have been explored, for example, with M = Ca,[6,7] Ti,[8,9] Fe,[10,11] Co,[12,13] Ru,[14,15] Ir,[16] In,[17,18] and rare earths Ln.[19–23] This led to the discovery of a range of M-cation ordered 10H perovskites $Ba_5In_{0.93}Mn_4O_{14.40}$,[17] $Ba_5Sn_{1.1}Mn_{3.9}O_{15}$,[24] $Ba_5Ce_{0.83}Mn_{4.17}O_{15}$,[25] and $Ba_5Sb_{1-x}Mn_{4+x}O_{15-\delta}$.[26] The $Ba_5MMn_4O_{15}$ 10H perovskite structure consists of close packed BaO_3 layers in a $(cchhh)_2$ sequence. The large M ions occupy the corner-sharing octahedral centre M1, and the Mn ions sit on the face-sharing octahedral centres M2 and M3, as shown in Fig. 1. Polymorphs of $BaMnO_{3-\delta}$ have long range antiferromagnetic (AFM) order of all the Mn spins, with T_N = 220–270 K.[4,5] However, the long-range magnetic order is suppressed in the 10H perovskites with low-level doping, and the metal occupying the corner-sharing M1 site plays a key role in the magnetic behaviour of these materials. $Ba_5In_{0.93}Mn_4O_{14.40}$ has diamagnetic In^{3+} ions on the M1 site and weak AFM interactions between the tetramers of face-sharing MnO_6 octahedra, and no magnetic order is observed down to 2 K. $Ba_5Sn_{1.1}Mn_{3.9}O_{15}$ (ref. 24) and $Ba_5Ce_{0.83}Mn_{4.17}O_{15}$ (ref. 25) have Mn^{4+} ions occupying 10–20% of the M1 sites and undergo spin glass transitions below 10 K. $Ba_5Sb_{1-x}Mn_{4+x}O_{15-\delta}$[26] phases have 24–36% M1 site occupancy by Mn^{3+} ions, and long range AFM order of partial Mn spins (moment ≈ 0.5 μ_B) below 129–167 K. The presence of Mn^{3+} ions on the M1 site causes ferro- or ferrimagnetic clusters to freeze below a second magnetic transition, in the temperature range 13–22 K.

The $BaLn_xMn_{1-x}O_3$ system contains several cation-ordered perovskites: 6H $Ba_3LnMn_2O_9$ and 12R $Ba_4LnMn_3O_{12}$ (Ln = Er, Ce, Pr, and Nd).[20–23,27] The 6H and 12R polytypes feature dimers and trimers of face-sharing MnO_6 octahedra respectively,[23,27] alternating with LnO_6 octahedra. The 6H and 12R perovskites

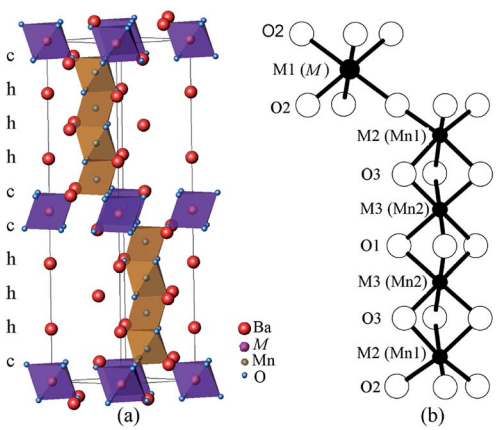

Fig. 1 10H $Ba_5MMn_4O_{15-\delta}$ perovskite structure (a) the unit cell and (b) the octahedral centres. The M ion is on the M1 site, and Mn ions sit on the M2 and M3 sites.

[a]College of Material Science and Engineering, Jiangxi University of Science and Engineering, Ganzhou, Jiangxi Province, 341000, P. R. China. E-mail: congling.yin@gmail.com

[b]Neutron Scattering Lab, Department of Nuclear Physics, China Institute of Atomic Energy, Beijing 102413, P. R. China

[c]Beijing National Laboratory for Molecular Sciences, State Key Laboratory of Rare Earth Materials Chemistry and Applications, College of Chemistry and Molecular Engineering, Peking University, Beijing 100871, P. R. China

† Electronic supplementary information (ESI) available. See DOI: 10.1039/c7ra02183f

are closely related to the 10H perovskite. Considering the similarity of Ln elements, we predicted the existence of 10H $BaLn_xMn_{1-x}O_3$ series and started an experimental exploration. Herein we report the syntheses, crystal structures and magnetic properties of 10H $Ba_5Ln_{1-x}Mn_{4+y}O_{15-\delta}$ (Ln = Sm–Lu) perovskites.

Experimental

Polycrystalline $Ba_5Ln_{1-x}Mn_{4+y}O_{15-\delta}$ samples were synthesised from $BaCO_3$, $MnCO_3$, and Ln_2O_3 (Ln = Sm–Gd and Dy–Lu) or Tb_4O_7. For each sample, the starting materials were thoroughly mixed in an agate mortar and pestle and heated in an alumina crucible at 1000 °C for 10 h to decompose the carbonates. Then the material was reground, pressed into pellets (20 ton per cm^2), and heated at 1300 °C for a total of 30–50 h with slow cooling to room temperature. At several intermediate steps the material was re-ground and re-pressed, and X-ray powder diffraction (XRPD) measurements were made at each step to track the reaction to completion.

The phase purity of the samples was checked by XRPD using a Rigaku D/Max-2000 diffractometer with graphite monochromator. This generated Cu Kα radiation at 40 kV and 100 mA. Data were collected over the 2θ range 6–120° in step scanning mode. Neutron powder diffraction data were collected using the BT-1 32 detector neutron powder diffractometer at the NIST Center for Neutron Research reactor, NBSR. A Cu (311) monochromator with a 90° take-off angle gave incident neutrons with $\lambda = 1.5403(2)$ Å, and in-pile collimation of 15 minutes of arc was used. Data were collected over the 2θ range 3–168° with a step size of 0.05°. The diffraction data were analysed with the GSAS program.[28] The Rietveld refinement was carried out assuming a pseudo-Voigt function for the peak shape and a calculated background using linear interpolation between a set of fixed points. Selected-area electron diffraction (SAED) were carried out on Tecnai G2 F30 with an accelerating voltage of 300 kV. The magnetic properties were investigated using a Quantum Design MPMS-SS superconducting quantum interference device (SQUID) magnetometer. Data were recorded in a 20 Oe or 1000 Oe applied field while warming the sample from 2–300 K, following both zero-field cooling (ZFC) and field cooling (FC).

Results and discussion

Chemical composition and 10H phase formation

The initial $Ba_5LnMn_4O_{15-\delta}$ samples consisted of mixed 10H and 12R phases. To eliminate the 12R phase, we first varied and found the Ln content that gave the lowest amount of a 12R phase. Then we fixed the Ln content at these values, and varied and optimised the Mn fractions. By repeating these optimisation steps for several cycles, 10H phase-pure samples were obtained with the Ba : Ln : Mn ratios listed in Table 1. Their general chemical formula is $Ba_5Ln_{1-x}Mn_{4+y}O_{15-\delta}$ (Ln = Sm–Lu).

Fig. 2 shows the XRPD patterns of the pure $Ba_5Ln_{1-x}Mn_{4+y}O_{15-\delta}$ samples, which are similar to that of $Ba_5Sb_{1-x}Mn_{4+x}O_{15}$.

Table 1 The optimised Ba : Ln : Mn ratios of the 10H $Ba_5LnMn_4O_{15-\delta}$ samples

Ln	Ba : Ln : Mn	Ln	Ba : Ln : Mn
Sm	5.00 : 0.98 : 4.01	Ho	5.00 : 0.86 : 4.12
Eu	5.00 : 0.87 : 4.02	Er	5.00 : 0.82 : 4.17
Gd	5.00 : 0.82 : 4.17	Tm	5.00 : 0.80 : 4.14
Tb	5.00 : 0.85 : 4.15	Yb	5.00 : 0.83 : 4.17
Dy	5.00 : 0.86 : 4.12	Lu	5.00 : 0.78 : 4.21

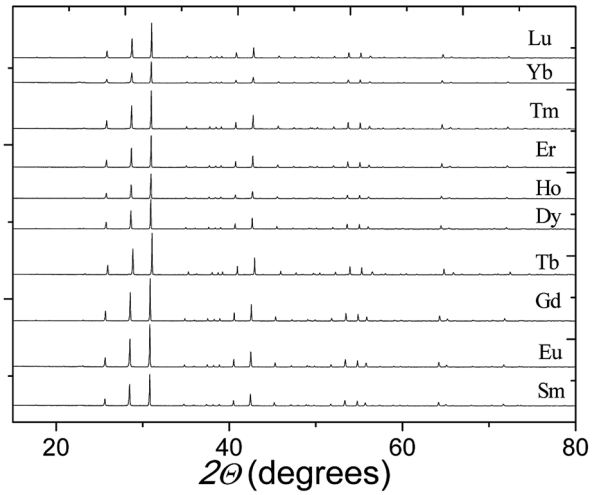

Fig. 2 X-ray diffraction patterns of our $Ba_5Ln_{1-x}Mn_{4+y}O_{15-\delta}$ samples, each showing a pure 10H perovskite phase.

The XRPD patterns of all our materials can be indexed using a hexagonal unit cell, with lattice parameters a = 5.76–5.80 Å and c = 23.75–24.04 Å. The Selected-Area Electron Diffraction (SAED) patterns collected on the $Ba_5Sm_{0.98}Mn_{4.01}O_{15-\delta}$ sample along [010], [0$\bar{2}$1] and [1$\bar{1}$0] zone axes are shown in Fig. 3. No superstructure reflections are seen, and all the observation reflections agree with the indexing results. The systematic absence of the reflections $hh\bar{2}\bar{h}l$: $l = 2n + 1$ is consistent with the space group $P6_3/mmc$.

The X-ray structures of $Ba_5Ln_{1-x}Mn_{4+y}O_{15-\delta}$

Rietveld refinement against the XRPD data was performed using the 10H $Ba_5Sb_{1-x}Mn_{4+x}O_{15}$ structural model. Ln ions and Mn ions occupy the M1 site, whilst the M2 and M3 sites are solely occupied by Mn. The ratio of Ln and Mn on the M1 site was fixed according to the ratio of reagents used. The refinements were insensitive to occupancies and isotropic thermal parameters of the oxygen sites, which were held at unity and 0.025 $Å^2$ respectively. Good fits were obtained with R_{wp} (weighted-profile residual) factors of 4.1–6.5% and χ^2 (goodness-of-fit) values in the range 1.7–3.0. The refined plots for all the sample are shown in ESI (Fig. S1–S10†). The refined crystallographic parameters and selected bond lengths are shown for all samples in Table S1.†

Across the $Ba_5Ln_{1-x}Mn_{4+y}O_{15-\delta}$ series, the lattice parameters and cell volume increase monotonically, in line with the

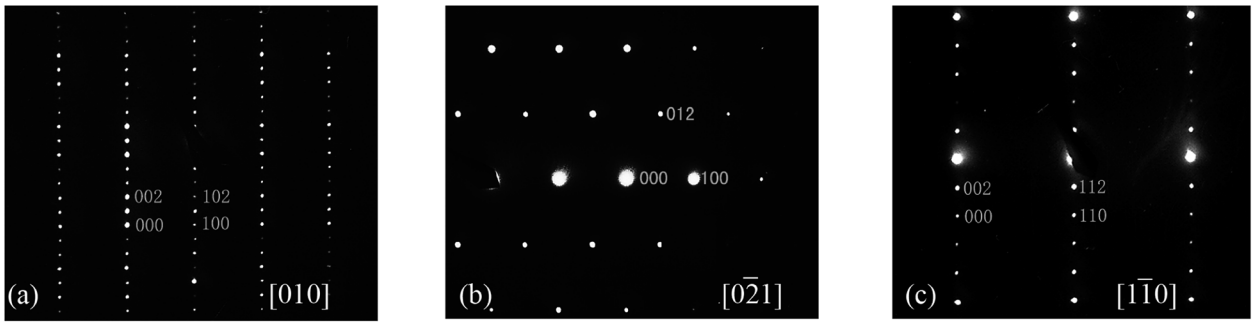

Fig. 3 SAED patterns of $Ba_5Sm_{0.98}Mn_{4.01}O_{15-\delta}$ along (a) [010], (b) [021], and (c) [110]. No superstructure is observed.

increasing ionic radius of the Ln^{3+} cation used. The sole exception is the Tb compound, which has considerably smaller lattice parameters and cell volume, as shown in Fig. 4. The refined Tb–O bond length (2.10 Å) is close to the calculated Tb^{4+}–O^{2-} length, indicating that the Tb ion is tetravalent. Tb^{4+} ions have also been found in the 12R perovskite series $Ba_4LnIr_3O_{12}$ and $Ba_4LnRu_3O_{12}$.[29,30]

All of our 10H perovskites have an ordered arrangement of Ln and Mn cations. Like the M = In^{3+} and Sb^{5+} 10H analogues, Mn ions alone occupy the octahedral centres that form face-sharing tetramers. These MnO_6 octahedra are distorted, with two sets of three Mn–O distances. For all our samples the Mn1 and Mn2 sites have very similar average Mn–O bond distances, of about 1.93 Å as shown in Fig. 5. This is the same as the Mn^{4+}–O^{2-} distance calculated from Shannon's radii,[31] indicating that the Mn ions in the sites forming tetramers of MnO_6 octahedra in the $Ba_5Ln_{1-x}Mn_{4+y}O_{15-\delta}$ phases is tetravalent. The Mn–Mn distances inside each tetramer range from 2.35 Å to 2.52 Å, close to the Mn–Mn distance in elemental α-Mn.[32] This observation may suggest a degree of d-orbital overlap between neighbouring Mn ions within each tetramer. The distortion of the MnO_6 octahedra forming the tetramers is evidenced by the fact that the Mn1–Mn2 distance is around 0.1 Å longer than the Mn2–Mn2 distance in all of our $Ba_5Ln_{1-x}Mn_{4+y}O_{15-\delta}$ samples.

The corner-sharing octahedral centre has mixed occupancy, with Ln ions in majority (more than 78%) and a minority of secondary Mn ions (less than 21%). Notably, the $Ba_5Ln_{1-x}Mn_{4+y}O_{15-\delta}$ samples are non-stoichiometric, with (Ln + Mn)/Ba values of 0.98–1. This non-stoichiometric associated with the vacancies at the M1 site (less than 10%), which has also been observed in $Ba_5In_{0.94}Mn_4O_{14.40}$.[17] As expected, the Ln–O distances increase with the size of Ln^{3+} except for the Tb-containing sample. The values are 10% smaller than the calculated Ln^{3+}–O^{2-} distances for all the samples, due to the partial occupation the M1 site by Mn.

Combined X-ray and neutron diffraction studies on $Ba_5Lu_{0.78}Mn_{4.21}O_{15-\delta}$

Due to their weak X-ray scattering, oxygen sites are not well described with PXRD. To find the exact oxygen positions and explore possible oxygen vacancies, we studied our sample of $Ba_5Lu_{0.78}Mn_{4.21}O_{15-\delta}$ using powder neutron diffraction. Rietveld refinements using X-ray and neutron diffraction data simultaneously were performed, starting from the refined X-ray structure. The oxygen occupancies were refined, and oxygen vacancies were found on the O2 site. The final refinement gave a good fit, with overall R_{wp} and χ^2 parameters of 6.4% and 2.3 respectively. The neutron refinement is shown in Fig. 6.

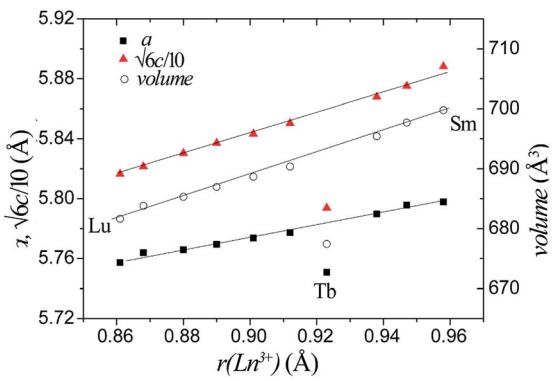

Fig. 4 The lattice parameters and unit cell volumes of all our $Ba_5Ln_{1-x}Mn_{4+y}O_{15-\delta}$ phases vary according to the radius of the Ln ion in each.

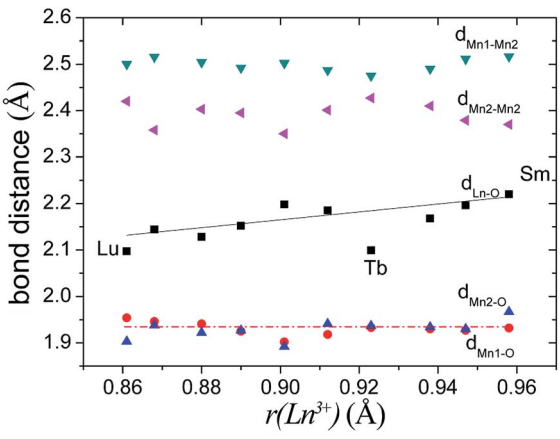

Fig. 5 Variations of the Ln–O, Mn–O and Mn–Mn distances in our $Ba_5Ln_{1-x}Mn_{4+y}O_{15-\delta}$ samples. d_{Mn1-O} and d_{Mn2-O} are average values. The solid and dashed lines indicate the trend for d_{Ln-O} and d_{Mn-O} values as r(Ln) increases.

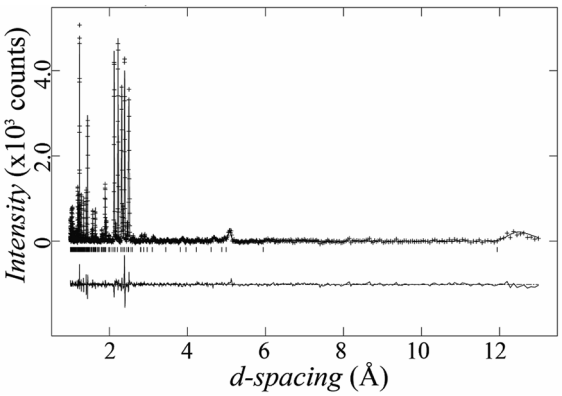

Fig. 6 Experimental and calculated neutron diffraction pattern of $Ba_5Lu_{0.78}Mn_{4.21}O_{15-\delta}$, with the difference plot offset below.

The refined atomic parameters are listed in Table 2. The O2 site in the c-BaO_3 layers is 6% vacant. Due to this oxygen deficiency, the O2 site has a larger thermal displacement factor than the O1 and O3 sites. The nearby sites Ba2 and M1 sites also have relatively large thermal factors.

From the refined occupancies, this material has the composition $Ba_5Lu_{0.78}Mn_{4.21}O_{14.64}$. The average valence state of Mn ions is found to be 4.0, and the Mn ions on the M1 site must also be Mn^{4+} ions in order to maintain electroneutrality. Our other $Ba_5Ln_{1-x}Mn_{4+y}O_{15-\delta}$ samples probably have Mn^{4+} ions on the M1 site as well, similar to the Ce^{4+} and Sn^{4+} analogues.[24,27] However, the $Ba_5Sb_{1-x}Mn_{4+x}O_{15-\delta}$ analogue is different with Mn^{3+} ions on the M1 site.[26] For the $BaM_xMn_{1-x}O_3$ 10H perovskites, the average valence of the cations occupying the M1 site approaches +4 in keeping with Pauling's principle.

The $Ba_5Lu_{0.78}Mn_{4.21}O_{14.64}$ sample has oxygen vacancy in the c-BaO_3 layers, which is similar to that in the In-doped analogue.[17] The M1 site in both compounds has a high occupancy of M^{3+} ions, which requires neighbouring oxygen vacancies to compensate the charge imbalance. When M^{4+} or M^{5+} ions dominate on the M1 site, oxygen vacancies in the c-BaO_3 layers are no longer present, as seen in the Ce^{4+}, Sn^{4+}, and Sb^{5+} analogues.[24–27]

In $Ba_5Lu_{0.78}Mn_{4.21}O_{14.64}$, the Mn_{M2}–O2 distance is 0.12 Å less than the Mn_{M2}–O3 distance, which indicates considerable distortion of the $Mn_{M2}O_6$ octahedron. In analogous materials with a small M ion, such as Sb^{5+}, the two Mn_{M2}–O distances are nearly equal and the $Mn_{M2}O_6$ octahedron is undistorted.[26] This indicates that the degree of $Mn_{M2}O_6$ distortion in the $Ba_5MMn_4O_{15-\delta}$ 10H perovskites is related to the size of M ion, r_M. The Mn–O distances are plotted against r_M in Fig. 7. The most noticeable trend is that M_{M2}–O2 distance shows a significant, linear decrease as r_M increases. The M_{M2}–O3 distance increases slightly with r_M.

For $Ba_5Lu_{0.78}Mn_{4.21}O_{14.64}$, the $Mn_{M3}O_6$ octahedron is almost undistorted, as evidenced by similarity of the two Mn_{M3}–O distances. This is similar to other 10H perovskites.

Table 2 Refined atomic parameters of $Ba_5Lu_{0.78}Mn_{4.21}O_{15-\delta}$ in space group $P6_3/mmc$ at 300 K[a]

Atom	x, y, z	Occup.	100× U Å^{-2}
Ba1	2/3, 1/3, 0.25	1	0.93(9)
Ba2	2/3, 1/3, 0.4422(1)	1	1.09(6)
Ba3	1, 0, 0.3437(1)	1	0.82(6)
M1 (Lu/Mn)	1, 0, 0.5	0.78/0/21	1.10(9)
M2 (Mn1)	1/3, 2/3, 0.4065(2)	1	0.83(11)
M3 (Mn2)	1/3, 2/3, 0.3010(2)	1	0.67(10)
O1	0.1836(4), 0.8164(4), 0.25	1	0.88(8)
O2	0.1765(3), 0.3530(6), 0.4486(1)	0.940(9)	1.36(8)
O3	0.4818(2), 0.9636(4), 0.3516(1)	1	0.80(6)

[a] Lattice parameters: $a = 5.7580(1)$ Å and $c = 23.7445(3)$ Å.

Magnetic properties

Low-temperature magnetic susceptibility data for our $Ba_5Ln_{1-x}Mn_{4+y}O_{15-\delta}$ materials are shown in Fig. 8. All are paramagnetic at high temperatures and show linear M–H variation, without hysteresis, at 300 K. The susceptibilities of the materials with Ln = Sm^{3+} and Eu^{3+} do not follow the Curie–Weiss law, due to the temperature dependent magnetic moments of these ions. The samples with Ln = Gd–Lu have susceptibility maxima at their spin freezing temperatures T_F = 3–34 K, and divergent ZFC and FC magnetic susceptibilities below T_F. In comparison to the samples containing an Ln^{3+} cation, which have around 15% Mn occupancy of the M1 site, the sample containing Tb^{4+} has a higher T_F = 34 K, which is due to anti-site dislocation of Mn^{4+} and Tb^{4+} ions on the M2 sites increasing the fraction of Mn on the M1 site. Mn^{4+}/M^{4+} site mixing has been observed in the other 10H $BaM_x^{4+}Mn_{1-x}O_3$ perovskites.[24,25] Curie–Weiss fits to the susceptibility above T_F give an effective paramagnetic moment μ_{eff} = 1.5–2.9 μ_B per Mn ion for the Ln = Gd–Lu samples (Table 3), which is smaller than that expected for localized Mn^{4+} spins (3.87 μ_B). Negative Weiss temperatures (θ = −2.5 K to −65 K) indicate that AFM interactions are dominant. Similarly small paramagnetic moments of 0.88–1.44 μ_B per Mn^{4+} ion, and large negative $\theta \approx -2000$ K, have reported in the 10H perovskite analogue $Ba_5Ce_{1-x}Mn_{4+x}O_{15}$.[25,27] This is probably due to the formation of AFM Mn clusters inside the tetramers, consistent with the observation of very short Mn–Mn

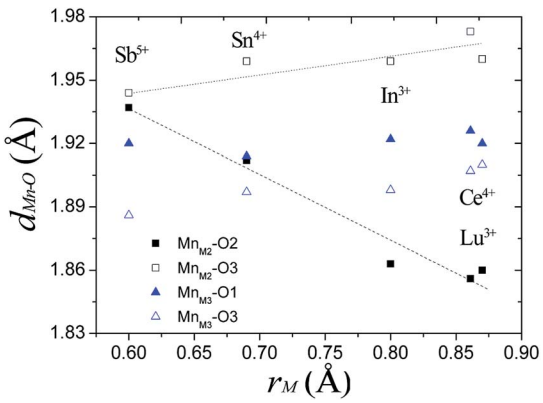

Fig. 7 The Mn–O distances of the face-sharing octahedra for several $Ba_5MMn_4O_{15-\delta}$ 10H perovskites vary with the radius of the M ion.

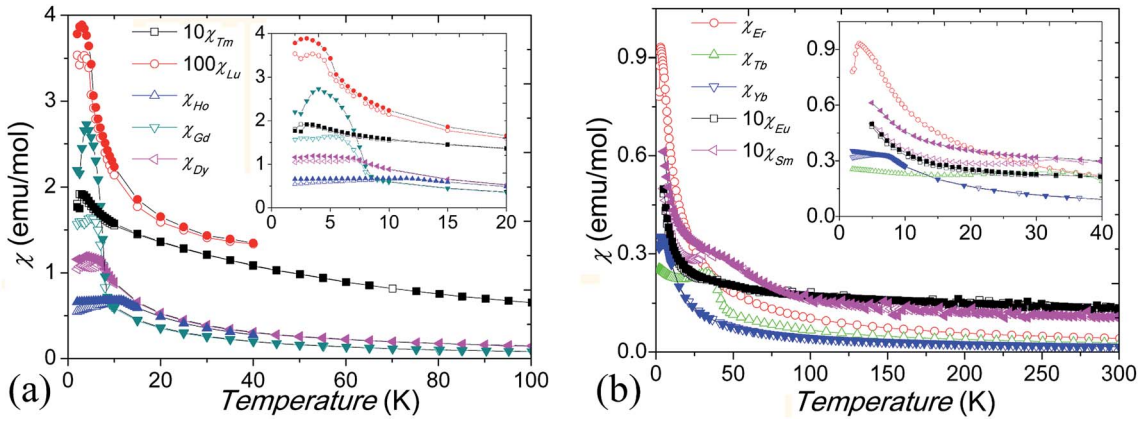

Fig. 8 Susceptibility χ *vs.* temperature for $Ba_5Ln_{1-x}Mn_{4+y}O_{15-\delta}$ (a) Ln = Tm, Lu, Ho, Gd, and Dy at 20 Oe; (b) Ln = Er, Tb, Yb, Eu, and Sm at 1000 Oe. The insets expand the low-temperature regions. Empty and filled symbols show ZFC and FC data, respectively. For clarity, χ are scaled by 10 for the Ln = Sm, Eu and Tm samples, and by 100 for the Lu sample.

Table 3 Magnetic ordering and Weiss temperatures, and effective paramagnetic moments and saturated magnetic moments, from susceptibility measurements of the $Ba_5Ln_{1-x}Mn_{4+y}O_{15-\delta}$ samples

Ln	Gd^{3+}	Tb^{4+}	Dy^{3+}	Ho^{3+}	Er^{3+}	Tm^{3+}	Yb^{3+}	Lu^{3+}
T_F/K	8.5	34.0	7.0	11.5	3.0	3.0	5.5	3.5
θ/K	−2.5	−39	−13	−7.2	−28	−52	−15.5	−65
μ_{eff} (f.u.)/μ_B	8.2	8.5	11.4	10.3	10.4	9.0	6.3	3.3
μ_{eff} (Ln)/μ_B	7.9	7.9	10.6	10.6	9.6	7.6	4.5	0
μ_{eff} (Mn)/μ_B	1.9	2.2	2.8	1.5	2.8	2.9	2.4	1.6
M_s (f.u.)/μ_B	0.3	0.05	1	0.8	0.5	0.06	0.05	0.05

distances and the significantly reduced magnetic moments of the Mn^{4+} ions.

Magnetic hysteresis and saturation occur at 2 K for the Ln = Gd–Lu samples, and the Gd^{3+}, Dy^{3+}, and Er^{3+} samples show history dependent magnetisation, as shown in Fig. 9. The Tb^{4+} and Yb^{3+} samples show small magnetic anisotropy with coercive fields of 20 mT at 2 K, and the other samples have isotropic magnetization, as shown in Fig. 9 inset. Due to the Mn ions in the tetramers forming AFM clusters, their total moments are almost zero at 2 K. The saturated moment M_s is therefore determined by the moments of the magnetic ions on the M1 site. The early Ln^{3+} samples have large M_s = 0.3–1 μ_B, close to that of ferromagnetic spin freezing Mn^{4+} cations on M1 site. The later Ln^{3+}, and Tb^{4+}, samples have a much smaller $M_s \approx$ 0.05 μ_B, similar to that of the Sn^{4+} and In^{3+} analogue materials.[17,24] This probably indicates AFM spin freezing of the Mn^{4+} ions on the M1 site. The different behaviours of the samples with early and late Ln cations reflects the changing difference in size between the Ln and Mn ions. A large size difference, as is found for the early Ln materials, tends to introduce oxygen vacancies and thus Mn^{3+} ions in the c-BaO_3 layers, resulting in a Mn^{3+}–O^{2-}–Mn^{4+} local ferromagnetic network and ferromagnetic spin freezing clusters.

Neutron diffraction data were collected for $Ba_5Er_{0.82}Mn_{4.17}O_{15-\delta}$ at 1.5 K, 10 K and 60 K, as shown in Fig. 10. No magnetic scattering is observed below the T_F = 3.0 K transition observed in the susceptibility, suggesting that this transition is due to short-range spin freezing, though further neutron studies, AC

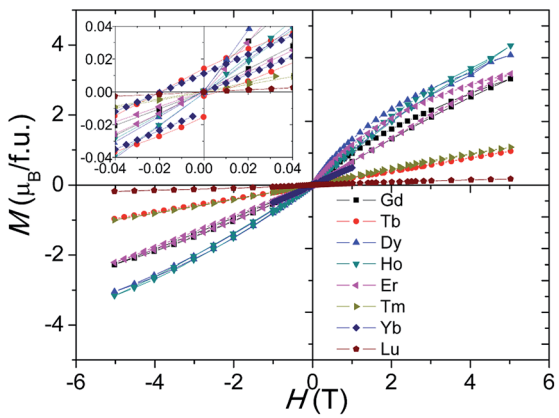

Fig. 9 Isothermal M–H curves at 2 K for the $Ba_5Ln_{1-x}Mn_{4+y}O_{15-\delta}$ (Ln = Gd–Lu) samples. The inset expands the low field region of the plot.

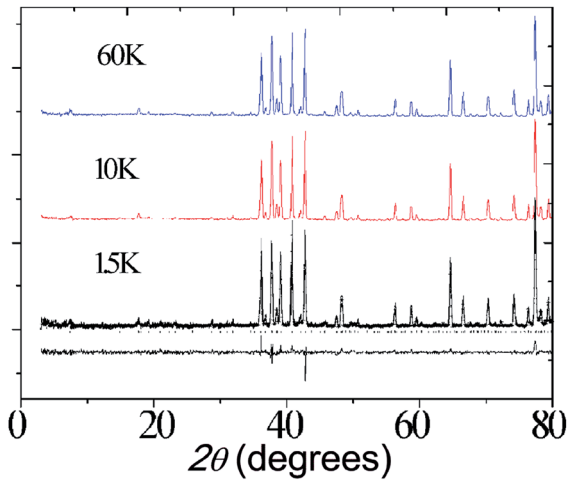

Fig. 10 Neutron diffraction profiles of $Ba_5Lu_{0.78}Mn_{4.21}O_{15-\delta}$ at different temperature. Fitting to the 1.5 K pattern is shown.

magnetic susceptibility measurements and μSR experiments will be useful in characterising this state more fully.

Conclusions

The new 10H perovskites $Ba_5Ln_{1-x}Mn_{4+y}O_{15-\delta}$ (Ln = Sm–Lu) have been synthesised by high temperature solid-state reactions. These materials have an ordered arrangement of Ln and Mn cations. The face-sharing octahedral centres are occupied by Mn^{4+} ions, whilst the corner-sharing octahedra are occupied by Ln and Mn cations. Oxygen vacancies are found in the c-BaO_3 layers. Within tetramers of MnO_6 octahedra, the two $Mn_{M2}O_6$ octahedra are distorted but the two $Mn_{M3}O_6$ octahedra are almost undistorted. The $Mn_{M2}O_6$ distortion is related to the size of the M ion in the $Ba_5MMn_4O_{15-\delta}$ 10H perovskite structure.

The $Ba_5Ln_{1-x}Mn_{4+y}O_{15-\delta}$ perovskites (Ln = Sm–Lu) are paramagnetic at high temperatures. The Ln = Gd–Lu samples have spin freezing transitions at $T_F = 3.0$–34 K, which have been characterised from their magnetic hysteresis at 2 K and low-temperature neutron diffraction. The spin freezing transition is related to the partial occupation of Mn^{4+} ions on the M1 sites of the 10H structure. The saturated moment is also related to the magnetic ions on the M1 site.

Acknowledgements

This work is supported by the National Natural Science Foundation of China (Grant 21271014, Grant 21301077 and Grant 51662013), and Scientific Research Key Program of Beijing Municipal Commission of Education (KM201010005019). We thank J. P. Attfield for the advice and encouragement and Alexander Browne for English modification. We acknowledge the support of the National Institute of Standards and Technology, U. S. Department of Commerce, in providing the neutron research facilities used in this work.

Notes and references

1 J. M. Gonzalez-Calbet, M. Parras, J. M. Alonso and M. Vallet-Regi, *J. Solid State Chem.*, 1993, **106**, 99.
2 T. Negas and R. S. Roth, *J. Solid State Chem.*, 1971, **3**, 323.
3 E. J. Cussen and P. D. Battle, *Chem. Mater.*, 2000, **12**, 831.
4 J. J. Adkin and M. A. Hayward, *Chem. Mater.*, 2007, **19**, 755.
5 J. J. Adkin and M. A. Hayward, *J. Solid State Chem.*, 2006, **179**, 70.
6 N. Floros, C. Michel, M. Hervieu and B. Raveau, *J. Solid State Chem.*, 2002, **168**, 11.
7 N. Floros, C. Michel, M. Hervieu and B. Raveau, *Chem. Mater.*, 2000, **12**, 3197.
8 G. M. Keith, C. A. Kirk, K. Sarma, N. M. Alford, E. J. Cussen, M. J. Rosseinsky and D. C. Sinclair, *Chem. Mater.*, 2004, **16**, 2007.
9 L. Miranda, A. Feteira, D. C. Sinclair, K. Boulahya, M. Hernando, J. Ramírez, A. Varela, J. M. González-Calbet and M. Parras, *Chem. Mater.*, 2009, **21**, 1731.
10 L. Miranda, J. Ramirez-Castellanos, M. Hernando, A. Varela, J. M. Gonzalez-Calbet and M. Parras, *Eur. J. Inorg. Chem.*, 2007, **15**, 2129.
11 L. Miranda, D. C. Sinclair, M. Hernando, A. Varela, A. Wattiaux, K. Boulahya, J. M. Gonzalez-Calbet and M. Parras, *Chem. Mater.*, 2009, **21**, 5272.
12 L. Miranda, A. Feteira, D. C. Sinclair, M. G. Hernandez, K. Boulahya, M. Hernando, A. Varela, J. M. Gonzalez-Calbet and M. Parras, *Chem. Mater.*, 2008, **20**, 2818.
13 L. Miranda, J. Ramirez-Castellanos, A. Varela, J. M. Gonzalez-Calbet, M. Parras, M. Hernando, M. T. Fernandez-Diaz and M. G. Hernandez, *Chem. Mater.*, 2007, **19**, 1503.
14 J. G. Zhao, L. X. Yang, Y. Yu, F. Y. Li, R. C. Yu and C. Q. Jin, *J. Solid State Chem.*, 2008, **181**, 1767.
15 C. L. Yin, G. B. Li, W. A. Kockelmann, J. H. Lin and J. P. Attfield, *Phys. Rev. B: Condens. Matter Mater. Phys.*, 2009, **80**, 094420.
16 N. A. Jordan and P. D. Battle, *J. Mater. Chem.*, 2003, **13**, 2220.
17 C. L. Yin, G. B. Li, T. N. Jin, L. P. You, J. L. Tao, J. W. Richardson, C. K. Loong, J. L. Sun, F. H. Liao and J. H. Lin, *Chem. Mater.*, 2008, **20**, 2110.
18 N. Creon, C. Michel, A. Hervieu, A. Maignan and B. Raveau, *Solid State Sci.*, 2003, **5**, 243.
19 X. J. Kuang, C. Bridges, M. Allix, J. B. Claridge, H. Hughes and M. J. Rosseinsky, *Chem. Mater.*, 2006, **18**, 5130.
20 H. Yang, Y. K. Tang, L. D. Yao, W. Zhang, Q. A. Li, F. Y. Li, C. Q. Jin and R. C. Yu, *J. Alloys Compd.*, 2007, **432**, 283.
21 H. Yang, Z. E. Cao, X. Shen, W. J. Feng, J. L. Jiang, J. F. Dai and R. C. Yu, *J. Mater. Sci.*, 2008, **43**, 5679.
22 A. F. Fuentes, K. Boulahya and U. Amador, *J. Solid State Chem.*, 2004, **177**, 714.
23 C. Rabbow and H. Mullerbuschbaum, *Z. Naturforsch., B: J. Chem. Sci.*, 1994, **49**, 1277.
24 C. L. Yin, G. B. Li, T. N. Jin, J. L. Tao, J. W. Richardson, C. K. Loong, F. H. Liao and J. H. Lin, *J. Alloys Compd.*, 2010, **489**, 152.
25 A. M. Mario, M. Olivier, C. Silviu, J. C. Gabriel and H. G. Gilles, *J. Solid State Chem.*, 2013, **198**, 186.
26 C. L. Yin, G. B. Li, W. A. Kockelmann, F. H. Liao, J. P. Attfield and J. H. Lin, *Chem. Mater.*, 2010, **22**, 3269.
27 A. M. Mario, M. Olivier, P. Caroline, R. Pascal, C. Silviu and H. G. Gilles, *New J. Chem.*, 2015, **39**, 829.
28 A. C. Larson and R. B. Von Dreele, Los Alamos National Laboratory Report, LAUR, 2004, pp. 86–748, unpublished.
29 Y. Shimoda, Y. Doi, Y. Hinatsu and K. Ohoyama, *Chem. Mater.*, 2008, **20**, 4512.
30 Y. Shimoda, Y. Doi, M. Wakeshima and Y. Hinatsu, *J. Solid State Chem.*, 2009, **182**, 2873.
31 R. D. Shannon, *Acta Crystallogr., Sect. A: Cryst. Phys., Diffr., Theor. Gen. Crystallogr.*, 1976, **32**, 751.
32 J. A. Oberteuffer and J. A. Ibers, *Acta Crystallogr., Sect. B: Struct. Crystallogr. Cryst. Chem.*, 1970, **26**, 1499.

